# *Neuronal activity drives pathway-specific depolarization of peripheral astrocyte processes*

HHS Public Access

Author manuscript

*Nat Neurosci*. Author manuscript; available in PMC 2023 March 06.

Published in final edited form as:

*Nat Neurosci*. 2022 May ; 25(5): 607–616. doi:10.1038/s41593-022-01049-x.

# Neuronal activity drives pathway-specific depolarization of peripheral astrocyte processes

**Moritz Armbruster**[1,*], **Saptarnab Naskar**[1], **Jacqueline P Garcia**[1,2], **Mary Sommer**[1], **Elliot Kim**[1], **Yoav Adam**[3,11], **Philip G Haydon**[1], **Edward S Boyden**[4,5,6,7,8,9], **Adam E Cohen**[3,10], **Chris G Dulla**[1,*]

[1]Department of Neuroscience, Tufts University School of Medicine, USA

[2]Cell, Molecular, and Developmental Biology Program, Tufts Graduate School of Biomedical Sciences, USA

[3]Department of Chemistry and Chemical Biology, Harvard University, USA

[4]Department of Brain and Cognitive Sciences, Massachusetts Institute of Technology, USA

[5]Department of Biological Engineering, Massachusetts Institute of Technology, USA

[6]McGovern Institute, Massachusetts Institute of Technology, USA

[7]Howard Hughes Medical Institute, Massachusetts Institute of Technology, USA

[8]Koch Institute, Massachusetts Institute of Technology, USA

[9]Center for Neurobiological Engineering, Massachusetts Institute of Technology, USA

[10]Department of Physics, Harvard University, USA

[11]Present address: Edmond and Lily Safra Center for Brain Sciences, the Hebrew University of Jerusalem, Israel.

## Abstract

Astrocytes are glial cells that interact with neuronal synapses via their distal processes, where they remove glutamate and potassium ($K^+$) from the extracellular space following neuronal activity. Astrocyte clearance of both glutamate and $K^+$ is voltage-dependent, but astrocyte membrane potential ($V_m$) has been thought to be largely invariant. As a result, these voltage-dependencies have not been considered relevant to astrocyte function. Using genetically encoded voltage indicators to enable the measurement of $V_m$ at peripheral astrocyte processes (PAPs) in mice,



*Correspondence: correspondence should be addressed to MA (Moritz.Armbruster@tufts.edu) or CD (Chris.Dulla@tufts.edu).

**Authors Contributions: Moritz Armbruster:** Conceptualization, Methodology, Investigation, Formal analysis, Data curation, Visualization, Writing -Original Draft. **Saptarnab Naskar:** Investigation, Formal Analysis, Writing – Review & Editing. **Jacqueline Garcia:** Investigation. **Mary Sommer:** Investigation. **Elliot Kim:** Investigation. **Yoav Adam:** Methodology, Investigation. **Phil Haydon:** Resources, Methodology. **Ed Boyden:** Resources, Methodology. **Adam Cohen:** Resources, Methodology. **Chris G. Dulla:** Conceptualization, Formal analysis, Visualization, Supervision, Funding acquisition, Project administration, Resources, Writing -Original Draft

**Competing interests:** The authors have no competing interests to disclose.

**Code availability:** All computer code used to collect and analyze data are available from the corresponding author on request.

we report large, rapid, focal, and pathway-specific depolarizations in PAPs during neuronal activity. These activity-dependent astrocyte depolarizations are driven by action potential-mediated presynaptic $K^+$ efflux and electrogenic glutamate transporters. We find that PAP depolarization inhibits astrocyte glutamate clearance during neuronal activity, enhancing neuronal activation by glutamate. This represents a novel class of sub-cellular astrocyte membrane dynamics and a new form of astrocyte-neuron interaction.

## Introduction

Astrocytes are glial cells with complex, ramified morphologies that enable their extensive physical interactions with synapses, blood vessels, and other cells. Nanometer scale astrocyte processes extend toward synaptic structures and are enriched in many functional astrocyte proteins. Excitatory amino acid transporters (EAATs; GLT1 and GLAST)[1], which remove extracellular glutamate and provide spatiotemporal control of excitatory neurotransmission, are concentrated in perisynaptic astrocyte processes. Likewise, the inward rectifying potassium ($K^+$) channel Kir4.1 is present at the fine processes where astrocytes contact synapses[2], helping to restore extracellular [$K^+$] after neuronal activity. EAAT function is strongly inhibited at depolarized membrane potentials[1], but whole cell recordings from astrocyte soma show that $V_m$ changes very little during neuronal activity (but see[3,4] for larger changes reported *in vivo* during synchronous activity and seizures). This has led to the assumption that astrocytes are electrically passive and undergo only very small changes in $V_m$. However, because astrocytes have very low membrane resistance ($R_m$), there is minimal spatial propagation of depolarization in astrocytes[5] and astrocyte morphology makes most of the astrocyte arbor inaccessible to electrophysiological recording. Therefore, we have no direct understanding of how $V_m$ changes outside of the astrocyte soma during neuronal activity. We suspected that astrocyte $V_m$ in the processes might be more dynamic than previously appreciated because EAAT function, which is reduced by membrane depolarization, is rapidly and reversibly inhibited by short bursts of neuronal activity[6,7]. Here we use genetically encoded voltage indicators (GEVIs) to demonstrate that neuronal activity induces large, rapid, focal, and pathway-specific depolarizations in peripheral astrocyte processes (PAP). Electron microscopy shows that astrocyte processes that directly interact with neuronal synaptic structures are ≈ 100 nm, below our resolution limits, so we use term PAP to broadly reference the fine astrocyte processes outside of astrocytic soma and primary processes. With that caveat in mind, we find that neuronal activity induces PAP depolarization primarily via elevated extracellular $K^+$, with glutamate transport playing a smaller, secondary role. Activity-induced PAP depolarizations inhibit glutamate transporter function, thereby increasing excitatory NMDA receptor-mediated neurotransmission onto cortical pyramidal neurons. Activity-induced PAP depolarizations represent a novel form of astrocyte-neuron communication and have important implications for understanding the role of astrocytes in shaping extracellular glutamate and $K^+$ dynamics. We anticipate that this finding will motivate further study of how $V_m$ modulates other astrocyte processes and how injury, inflammation, and disease alter this fundamental aspect of astrocyte function.

## Results

### GEVIs show fast activity-dependent astrocyte depolarization.

We expressed the GEVIs Archon1-EGFP[8] or Arclight[9] in layer II/III mouse cortical astrocytes using AAV-mediated transduction under the control of a modified GFAP promoter[10]. Immunohistochemical studies show robust GEVI expression co-localized with the astrocyte marker glutamine synthase (GS), but not with the neuronal marker NeuN (Fig. 1A, B). Transduced astrocytes were morphologically reconstructed (AAV5-GFAP-tdTomato or EAAT2-tdTomato mice[11]) and GEVI expression was seen throughout the astrocyte arbor (Fig. 1C, Ext. Fig. 1, 2). Transduced astrocytes showed low GFAP expression and were morphologically similar to un-transduced astrocytes, consistent with minimal reactive astrogliosis (Ext. Fig. 1, 2). This confirms that our approach enables the imaging of $V_m$ throughout the astrocyte arbor.

Acute coronal brain slices were then prepared and somatic whole cell recordings were made from layer II/III astrocytes while ascending cortical axons were activated via electrical stimulation (1, 5, or 10 stimuli at 100 Hz). Consistent with previous reports, small somatic depolarizations were seen with stimulation (Fig. 1D). The amplitude of somatic depolarization increased with the number of stimuli delivered. Next, GEVI imaging of layer II/II astrocytes was performed using spinning disk confocal microscopy. Stimulus-evoked changes in astrocyte GEVI $\Delta F/F_0$ were quantified and both Archon1 and Arclight showed stimulus-evoked changes in $\Delta F/F_0$, consistent with astrocytic depolarization (Archon1: $\uparrow \Delta F/F_0$, Arclight: $\downarrow \Delta F/F_0$ = Depolarization). GEVI $\Delta F/F_0$ amplitude increased with stimuli number (Fig. 1E, F, H, I), similar to somatic electrophysiological recordings of $V_m$.

We next examined the decay time of activity-induced astrocyte depolarizations monitored using GEVIs, versus those recorded electrophysiologically at the soma. Because Arclight is based on pHluorin, it undergoes pH-dependent quenching of fluorescence[12], interfering with quantification of $\Delta V_m$ kinetics. To correct this pH-effect, pHluorin quenching was imaged in separate experiments using a cytosolic-facing membrane-targeted pHluorin construct (AAV5-GFAP-Lyn-mCherry-pHluorin)[13], mimicking pHluorin's position in the Arclight construct. pHluorin imaging revealed pH-dependent changes in $\Delta F/F_0$ that were used to correct Arclight signals for changes in pH (Ext. Fig. 3). Both Archon1 and pH-corrected Arclight showed $\Delta V_m$ $T_{1/2}$ decay times of approximately 200 ms (Archon: $T_{1/2}$ = 211.2 ± 24.3 ms, n = 33 slices/8 mice; Arclight: $T_{1/2}$ = 197.3 ± 30.9 ms, n = 11 slices/3 mice), while $T_{1/2}$ decay times of depolarization measured with somatic whole cell recording was ≈ 5-fold slower (1206.8 ± 234.7 ms, n = 5 cells/3 mice, Fig. 1J, K). This suggests that voltage changes measured using GEVIs have distinct kinetic properties from those measured electrophysiologically at the soma. Because most astrocyte membrane is found in processes, membrane targeted probes predominantly report activity in astrocyte processes[14]. In fact, confocal imaging shows that only ≈ 1% of Arclight fluorescence originates from the astrocyte soma (Ext. Fig. 4). Therefore, we suspected that GEVI signal may be heavily biased to astrocyte process $V_m$.

### Astrocyte depolarizations are focal and spatially stable.

We next used principal component analysis/independent component analysis (PCA/ICA)[15] to identify regions of depolarization in astrocytes using both Archon1 and Arclight. This identified small "hotspots" that were used as regions of interest (ROIs) for GEVI analysis (Fig. 2A, B, Sup. Fig. 1, 2, supplemental methods). Stimulus-evoked $\Delta F/F_0$ in these hotspots was significantly enhanced, compared to all other regions within the imaged area (Fig. 2C–F) and were stable over repeated trials (Fig. 2G). Detected ROIs were extremely focal (Archon: 0.36 ± 0.02 $\mu m^2$, n=10 slices/5 mice; Arclight: 0.49 ± 0.15 $\mu m^2$, n=17 slices/6 mice), with similar size distributions for both GEVIs (Fig. 2H–J), suggesting they may originate from PAPs. Kymographs also confirmed spatially restricted depolarizations (Arclight: FWHM = 446±7 nm, n = 8 slices/5 mice; Archon: FWHM = 572 ± 17 nm, n = 9 slices/4 mice, Fig. 2H–I). These spatial measurements reflect a combination of the depolarization size, the spatial size of astrocyte processes, and the optical limitations of our microscopy approaches. As a result, our estimates of GEVI hotspot FWHM are likely an over-estimate of the physical size of the underlying depolarization but are consistent with depolarization originating from PAPs.

To identify the location of activity-induced GEVI hotspots within the astrocyte arbor, we co-infected GEVIs with AAV5-GFAP-tdTomato to fluorescently identify astrocyte soma and primary processes. Additionally, we switched imaging modalities to a confocal line-scanning microscope with improved confocality by avoiding pinhole crosstalk that occurs in spinning disk microscopy. Using this approach, we found that GEVI hotspots were found primarily outside of the astrocyte soma and primary processes (Fig. 3A, B). A small number of hotspots were located on soma/primary processes, but we suspect these represent closely co-incident fine processes[14] that cannot be resolved with our axial/spatial resolution. Consistent with astrocyte PAP depolarizations, GEVI signal was significantly enhanced in hotspot ROIs compared to ROIs containing the astrocyte soma and primary processes (Fig. 3C, E). When we examined the spatial distribution of GEVI hotspots, we found that they were broadly distributed across the astrocyte arbor (Fig. 3D, F), again consistent with PAP depolarizations.

To further understand hotspot morphology, we quantified their individual spatial properties. Interestingly, hotspots were asymmetrical with a long and short axis (Fig. 3, Ext. Fig. 5). We created an average GEVI hotspot profile by aligning individual hotspots along their long axis. We found the GEVI hotspots were small and asymmetrical (FWHM, Arclight: 637 ± 20 nm *short dimension*, and 1518 ± 34 nm *long dimension*; Archon: 545 ± 15 nm *short dimension* and 1380 ± 29 nm *long dimension*, Fig. 3G/H). The small dimensions of the hotspot FWHM were similar to what was observed with spinning disk imaging, where rotational alignment was not possible due to signal to noise. The large dimension likely occurs due to a spatial spread of depolarization along PAPs and is consistent with an astrocyte membrane space constant of ~3 μm[5,16]. We fit individual ROI hotspots to calculate their spatial properties along both axes and found that hotspots showed significantly more skewed along the long axis (Y-axis) (Ext. Fig. 5). This is in-line with the depolarization initiating at the tip of astrocyte processes and spreading unidirectionally along the long axis. Given the limitations of our spatial resolution and the size of astrocyte fine processes,

however, new approaches will need to be developed to conclusively determine the precise subcellular and sub-process localization of astrocyte depolarizations within PAPs.

### Astrocyte depolarizations are pathway specific.

We next performed Arclight GEVI imaging using our standard high speed spinning disk confocal approach while delivering electrical stimulation to either ascending cortical axons or LII/III intracortical axons (Fig. 4A)[6]. Hotspots were identified for each stimulation pathway using PCA/ICA. Interestingly, there was minimal spatial overlap of astrocyte depolarization hotspots evoked by ascending and intracortical axons (Fig. 4B). ROIs identified from stimulation of ascending axons showed minimal responses when intracortical axons were stimulated, and vice-versa (Fig. 4C, D). Archon1 imaging replicated the pathway-specific enrichment of $\Delta F/F_0$ results (Fig. 4E). Together, this demonstrates that stimulus-induced astrocyte depolarization is pathway specific and could provide a mechanism to drive synapse-specific modulation of glutamate uptake and other astrocyte functions [6].

### Calibrating GEVI signal in PAPs.

We next estimated the $\Delta V_m$ associated with $\Delta F/F_0$ using a straight-forward calibration approach. This and subsequent experiments were performed using exclusively Arclight, due to its better signal-to-noise characteristics in our assay. In separate experiments, we measured astrocyte somatic $V_m$ using electrophysiology and PAP GEVI fluorescence while increasing $[K^+]$ in the extracellular solution. This should induce a spatially uniform depolarization of both astrocyte processes (Ext. Fig. 6) and soma. As predicted, increasing extracellular $[K^+]$ depolarized somatic $V_m$ (Fig. 5A) and altered GEVI fluorescence (Fig. 5B). We performed a linear fit of the Arclight $\Delta F/F_0$ and somatic $\Delta V_m$ in response to increasing extracellular $[K^+]$ by 5 mM and 10 mM (Linear fit with fixed intercept $R^2 = 0.988$). Using this calibration, we estimate that the $\Delta F/F_0$ seen in PCA/ICA-identified hotspots reflects depolarizations of 19.2 ± 2.1 mV in response to 10 stimuli at 100Hz, approximately 10-fold more than is seen at the soma (Fig. 1D). The same calibration approach suggest that non-hotspot regions depolarize by 5.1 ± 0.8 mV (n = 17 slices/6 mice).

### Presynaptic activity drives astrocyte depolarization via $K^+_e$ and EAATs.

To determine the mechanisms that drive PAP depolarization, we probed the effects of neuronal activity, post-synaptic glutamate receptor activity, EAAT activity, and modulating $K^+$ homeostasis on GEVI $\Delta F/F_0$. Tetrodotoxin, which blocks voltage-gated sodium channels, eliminated stimulus-evoked GEVI $\Delta F/F_0$, confirming that neuronal activity is required (Fig. 6A). This also eliminated the possibility that electrical stimulation acts directly on PAPs to drive their depolarization. We next assayed the role of glutamate receptor activation in PAP depolarization by blocking both AMPA and NMDA receptors (DNQX 20 μM, AP-5 50 μM, respectively). This had no effect on GEVI $\Delta F/F_{0,}$ showing that AMPA and NMDA receptor activation does not contribute to PAP depolarization in this setting (Fig. 5B). Next, we tested whether EAAT-mediated glutamate uptake, which carries an inward, depolarizing current, contributes to activity-induced PAP depolarization. Blocking EAATs with TFB-TBOA (1 μM) partially reduced GEVI $\Delta F/F_0$ (Fig. 6C). Interestingly, the effect of EAAT blockade

was similar for 5 and 10 stimuli (Fig. 6G), consistent with suppression of glutamate release during prolonged trains of neuronal activity [6,7]. This also suggests that other mechanisms drive the increased GEVI $\Delta F/F_0$ seen with increasing number of stimuli.

Because astrocyte $V_m$ is highly dependent on $[K^+]_e$ and neuronal activity increases $[K^+]_e$ [17], we tested whether manipulating astrocyte $K^+$ handling alters activity-dependent PAP depolarization. The astrocytic inwardly rectifying $K^+$ channel, Kir4.1, is the primary mediator of activity-dependent astrocyte $K^+$ buffering [18] and can be blocked with 200 μM $Ba^{2+}$ [19]. Viral overexpression of Kir4.1 (Kir4.1-OE)[20–22] (AAV5-GFAP-Kir4.1-mCherry or AAV5-GFAP-Kir4.1-EGFP, Ext. Fig. 7) significantly reduced GEVI $\Delta F/F_0$ for both 5 and 10 stimuli (Fig. 6D). Unlike the effects of EAAT inhibition, the effect size of Kir4.1 overexpression on GEVI $\Delta F/F_0$ was significantly larger for 10 stimuli, as compared to 5 stimuli (Fig. 6G). Conversely, inhibiting Kir4.1 with $Ba^{2+}$ caused a small but significant increase in GEVI $\Delta F/F_0$ (Fig. 6E), suggesting that Kir4.1-mediated $K^+$ influx helps to minimize activity dependent PAP depolarization. Conversely, $Ba^{2+}$ blockade of Kir4.1 reduces stimulus-evoked depolarization of the soma measured via whole cell electrophysiology [18,23] (Ext. Fig. 8). We next tested whether the effects of Kir4.1-OE and TFB-TBOA were additive. TFB-TBOA reduced activity-dependent GEVI $\Delta F/F_0$ even when Kir4.1 was overexpressed, confirming that EAAT activity and changes in $[K^+]_e$ represent distinct mechanisms contributing to PAP depolarization. This suggests that activity-dependent accumulation of extracellular $K^+$ is the primary driver of stimulus-dependent PAP depolarization, while EAAT activity plays a secondary role.

Finally, we asked whether reducing extracellular $Ca^{2+}$ (which can affect presynaptic function, membrane charge screening, and $Ca^{2+}$ signaling) altered activity-dependent changes in GEVI $\Delta F/F_0$. Reducing extracellular $[Ca^{2+}]$ from 2 mM to 1 mM had a strong effect on GEVI $\Delta F/F_0$ rise-time, due to a delayed onset of depolarization (Sigmoidal $T_{1/2}$ rise time for 10 Stimuli 100Hz: 61.3 ± 3.6 ms Control; 85.1 ± 5.9 ms Low $Ca^{2+}$; Paired t-test $p = 0.0013$) and caused a small but significant decrease in PAP $\Delta V_m$ peak (Fig. 6H). While lowering $Ca^{2+}$ decreases glutamate release, glutamate receptor activation does not drive PAP depolarization (Fig. 6B) and low $Ca^{2+}$ effects on presynaptic release are not correlated with the effects on PAP depolarization (Ext. Fig. 9). This suggests that activity dependent changes in PAPs can be altered by lowering extracellular $Ca^{2+}$, but the precise mechanisms are unclear. We suspect a membrane charge screening [24] meditates the effects of lowered extracellular $Ca^{2+}$ on PAP depolarization, but other potential mechanisms ($Ca^{2+}$ signaling, $Ca^{2+}$ activated $K^+$ channels) exist.

### PAP $V_m$ modulates glutamate clearance and NMDAR activation.

The results we report suggests voltage-dependent modulation of astrocyte function may occur in PAPs. Astrocyte glutamate clearance by EAATs is rapid (<10 ms)[25], steeply inhibited by depolarization in expression systems[1], and slowed by neuronal activity in cortical brain slices[6,7]. We therefore hypothesized that EAAT function may be modulated in astrocytes by activity-induced PAP depolarization. To test this hypothesis, we used approaches that alter activity-induced PAP GEVI $\Delta F/F_0$ (Fig. 6) and asked whether these manipulations affect the stimulus-dependent slowing of EAAT function and glutamate

clearance. Using iGluSnFr glutamate imaging [6,26] and NR2A-specific NMDA currents [6], we tested the effects of Low $Ca^{2+}$ (Fig. 7A, B), $Ba^{2+}$ (Fig. 7C, D), and Kir4.1-OE (Fig. 7E, F) on activity-dependent inhibition of glutamate clearance. Kir4.1-OE and Low $Ca^{2+}$, which reduce PAP GEVI $\Delta F/F_0$ (Fig. 6D, H), both reduced the slowing of glutamate clearance associated with trains of neuronal activity. The slowing of glutamate clearance is independent of the amount of glutamate released[6] (Ext. Fig. 9), suggesting that the effects of low $Ca^{2+}$ are not mediated by reduced presynaptic glutamate release. Recording astrocyte glutamate transporter currents (GTCs) confirmed that lowering $Ca^{2+}$ reduced activity-dependent inhibition of EAAT function (as assayed by GTC decay times, Ext. Fig. 10). Conversely, blocking Kir4.1 with $Ba^{2+}$, which augments PAP GEVI $\Delta F/F_0$ (Fig. 6E), enhanced the activity-dependent slowing of glutamate clearance (Fig. 7C, D). These experiments show that activity-dependent astrocyte depolarization inhibits EAAT function.

## Discussion

Using GEVI imaging, we show that astrocytes undergo highly focal depolarizations ($\Delta V_m \approx 20$ mV) during brief bouts of neuronal activity. These depolarizations occur with pathway specificity, are driven by a combination of presynaptic $K^+$ release and EAAT activity, and impact activity-induced slowing of glutamate uptake. These results challenge the view that astrocytes have largely invariant membrane potential and show that local astrocyte depolarizations have functional effects on EAAT activity and glutamate neurotransmission. Our data supports that GEVI detected changes in $V_m$ occur largely in astrocyte PAPs, outside the astrocyte soma and primary processes. Although optical limitations prevent us from conclusively saying that GEVI hotspots represent astrocyte processes directly adjacent to synapses, multiple pieces of evidence suggest they do. Depolarizations are driven by both presynaptic neuronal activity and glutamate transport and shape synaptic glutamate dynamics. The spatial properties of activity-induced GEVI hotspots shows that they are asymmetrical and are skewed along their long axis, consistent with depolarizations that initiate at the tips of astrocyte processes. Although these data suggest that astrocyte depolarizations occur at processes adjacent to synapses, caveats of live imaging in nanometer scale processes make this difficult to confirm using our current approaches. Additionally, multiple mechanisms contribute to the morphological properties of the PAP depolarizations we report, including the astrocyte membrane space constant (~3 μm[5,16]), the spatial relationship between astrocyte and neuronal processes, the location of $K^+$ release, and $K^+$ diffusion in the extracellular space. Our results, therefore, may overestimate the spatial extent of PAP depolarization (FWHM ≈ 500nm Fig. 2H, I, 3G, H, Ext. Fig. 5) and underestimate their peak amplitude. These caveats aside, our findings show that astrocytes undergo large, rapid, and focal voltage changes during neuronal activity.

Elevation of $[K^+]_e$ appears to be a significant driver of activity-induced PAP depolarization. Astrocyte $V_m$ is largely set by $[K^+]_e$, but the spatial nature of $[K^+]_e$ dynamics are not well understood. Our findings predict that neuronal activity induces highly focal increases in $[K^+]_e$ on the magnitude of ≈ 10 mM in response to neuronal electrical stimulation. This is significantly larger than generally reported during brief bursts of neuronal activity, but the small spatial scale of the predicted elevations in $[K^+]_e$ would be difficult to resolve using previous approaches like $K^+$-selective electrodes. During prolonged activity (>30 s)

or pathological states, like seizures, $[K^+]_e$ can increase to ≈ 10 mM, making our reported measurement physiologically possible[17,27]. The small spatial nature of the depolarizations we report may have important implications on astrocytic $K^+$ buffering. Locally elevated $[K^+]_e$ depolarizes astrocytes, as modeled by the Nernst potential/Goldman-Hodgkin-Katz equation. As Kir4.1-mediated $K^+$ influx helps $[K^+]_e$ levels return to baseline, astrocyte $V_m$ locally recovers. Therefore, blocking Kir4.1 enhances PAP depolarizations (Fig. 6), presumably by increasing and prolonging activity-induced changes in $[K^+]_e$. At the soma, $[K^+]_e$ changes very little (Fig. 3, Ext. Fig. 8), so small, slow somatic astrocyte depolarization is likely driven by Kir4.1-mediated inward $K^+$ currents occurring throughout the cell, rather than local Nernstian-driven depolarization. In this situation, inhibition of Kir4.1 blocks the depolarizing inward current and reduces activity-induced astrocyte depolarization measured at the soma[18,23] (Ext. Fig. 8). Future development of $K^+_e$ imaging approaches and computational modeling of astrocytes[16] will continue to improve our understanding of the focal and dynamic nature of activity-induced astrocyte depolarization and astrocytic $K^+$ buffering.

Astrocytic glutamate uptake by EAATs is voltage-dependent and inhibited by neuronal activity. Our data supports that PAP $V_m$ shapes EAAT function during neuronal activity. Modulating PAP $V_m$, by altering $[K^+]_e$ handing, can bidirectionally shape extracellular glutamate dynamics and NMDA receptor decay times. Altering PAP $V_m$ has a significant, but relatively small, effect on EAAT function, suggesting that either our manipulations do not sufficiently control PAP $V_m$ or that other changes (EAAT trafficking[28], cell swelling, diffusion, pH changes) play a large role in activity-dependent inhibition of EAAT function. We are unable to depolarize PAPs to directly test the correlation of glutamate clearance slowing and depolarization due to technical limitations (small astrocyte space clamp and confounding ionic changes due to EAAT dependence on $Na^+$, $K^+$, and $H^+$). As a result, modulations of $V_m$ and glutamate clearance are limited to correlative changes. Interestingly, neither activity-dependent EAAT inhibition nor PAP depolarization relies on glutamate receptor activation. This is surprising as post-synaptic NMDA receptor activation has been shown to mediate $K^+$ efflux, which should depolarize astrocytes [29]. This could represent ultrastructural differences in $K^+$ handling at PAPs and soma or brain region-specific astrocyte-neuron interactions. Our findings could also have important implications on astrocyte-neuron interactions and on the role astrocyte depolarization may play in activity-dependent synaptic plasticity[30].

How PAP depolarization affects other astrocytic functions remains to be seen, but astrocytes have complex intracellular $Ca^{2+}$ signaling and express voltage-dependent ion channels [31–34], receptors [35], and transporters[36] that may be functionally modulated by $V_m$. Additionally, experimental manipulations such as channelrhodopsin can increase $[K^+]_e$ [37] which may affect astrocyte $V_m$. Finally, astrocytes are highly dynamic, responding to injury, inflammation, and more. If PAP properties are altered during reactive astrocytosis, the coupling between neuronal activity and astrocyte function may be altered, especially during behaviorally relevant bursts of neuronal activity in vivo. Together, this study shows that astrocytes experience rapid, focal, and functionally relevant depolarizations during neuronal activity.

## Extended Data

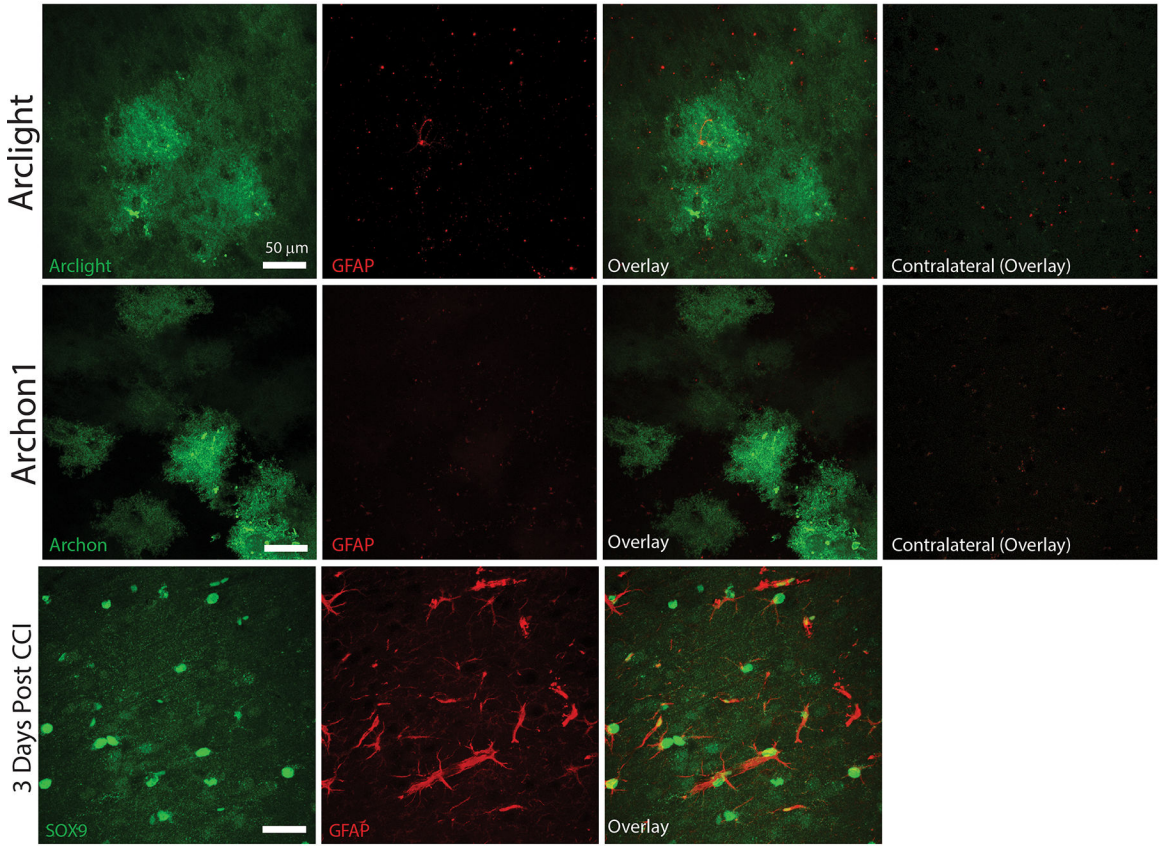


**Extended Data Fig. 1. GEVI expression does not induce reactive astrocytosis.**
Representative confocal IHC images stained for GFAP in Arclight infected and Archon1-EGFP (EGFP fluorescence shown) infected cortices. Additionally, staining in matched uninfected contralateral cortex. Neither GEVI infected or uninfected contralateral cortex shows high GFAP levels, indicative of a lack of reactive astrocytosis. In order to verify the sensitivity of our GFAP antibody, we stained slices 3 days following controlled cortical impact, a robust model of traumatic brain injury. In this positive control, astrocytes are labeled with the astrocyte specific marker Sox9 and shows high levels of GFAP staining and astrocytosis. Scalebar = 50 μm.

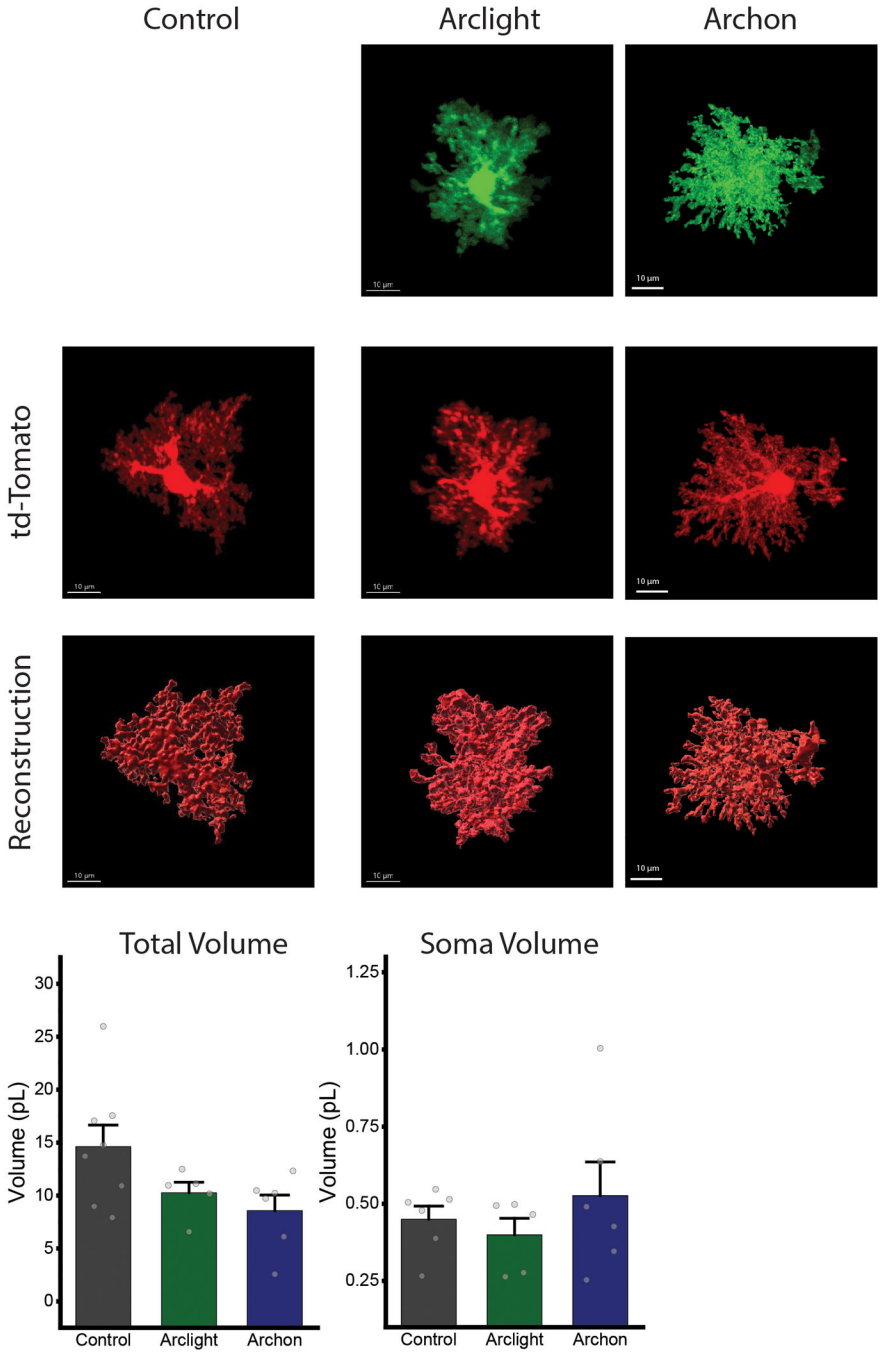


**Extended Data Fig. 2. GEVI expression does not change astrocyte morphology.**
Example confocal sections and reconstruction of the astrocyte cell-fill reporter tdTomato either uninfected controls (left column), Arclight infected (middle column), or Archon infected (right column). No significant changes were observed in total astrocyte volume or soma volume between control or GEVI infected astrocytes. N= 8 control, 5 Arclight, 6 Archon astrocytes. One way ANOVA Control v Arclight p = 0.23, Control v Archon p = 0.058, Arclight v Archon p = 0.81. All panels: Error bars = Standard error of the mean.

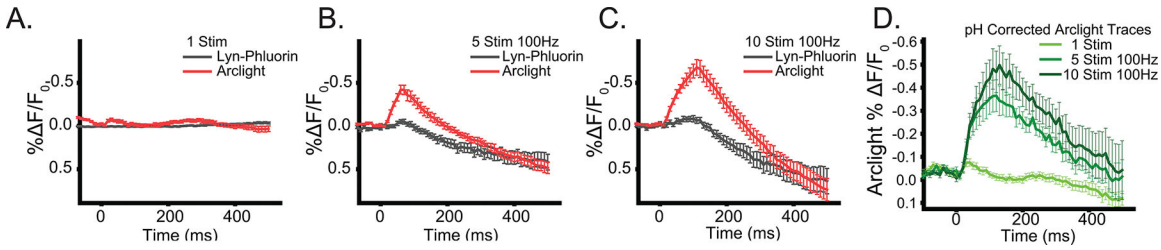


**Extended Data Fig. 3. Correcting pH transients.**

Average pH transients (Lyn-pHluorin) and Arclight GEVI responses to A) 1 Stim, B) 5 Stimuli at 100Hz, C) 10 Stimuli at 100Hz. D) The GEVI decays are corrected for the pH changes using the difference in the Arclight and pHluorin traces. n = 9 Slices/ 3 mice (pHluorin). n = 17 slices/6 mice (Arclight). All panels: Error bars = Standard error of the mean.

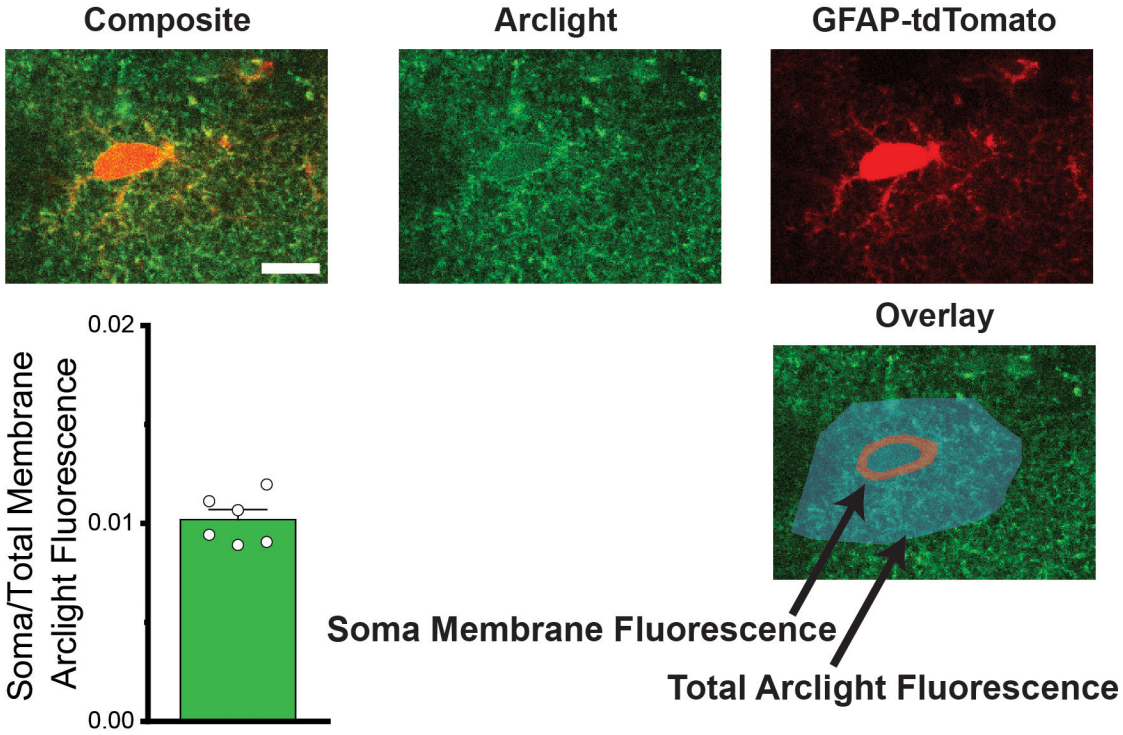


**Extended Data Fig. 4. Astrocyte membrane probes primarily localize to astrocyte process rather than soma.**

Example confocal images from a 3D Z-stack of astrocyte targeted Arclight (a membrane targeted GEVI) and an astrocyte cell fill (GFAP-tdTomato). We subsequently quantified the Arclight fluorescence originating from the soma membrane compared to the total astrocyte Arclight fluorescence in all Z-sections. Soma fluorescence represents 1.0 ± 0.0005% of the total Arclight fluorescence N = 6 astrocytes. Scale bar = 10 μm.

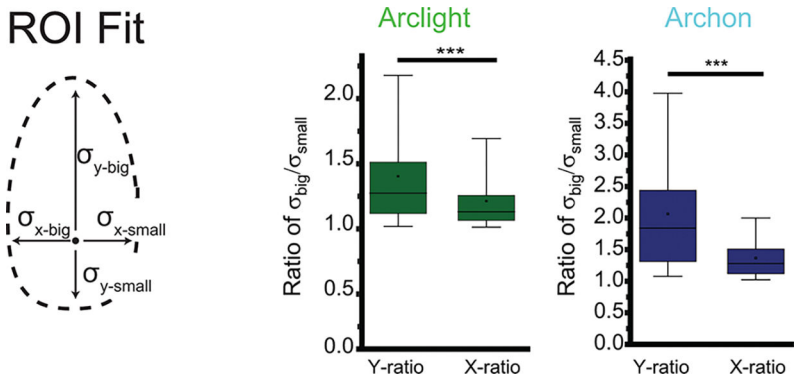


**Extended Data Fig. 5. Confocal Laser Scanning Microscopy shows ROI hotspots have skewed distributions.**

Half of individual ROI hotspots from Fig. 3G/H, are fit with 2D gaussians to determine one-sided standard deviations for X and Y- axis. Both Arclight and Archon show significantly more skewed fluorescence distribution along the Y-axis. Box-Whisker plot, Box = 25, 50, 75$^{th}$ percentile, whiskers = 5–95$^{th}$ percentile, square = mean. *** = $p < 0.001$. N= 1109 ROIs (Arclight, p = 1.1E-30) and N=104 ROIs (Archon p = 3.3E-11).

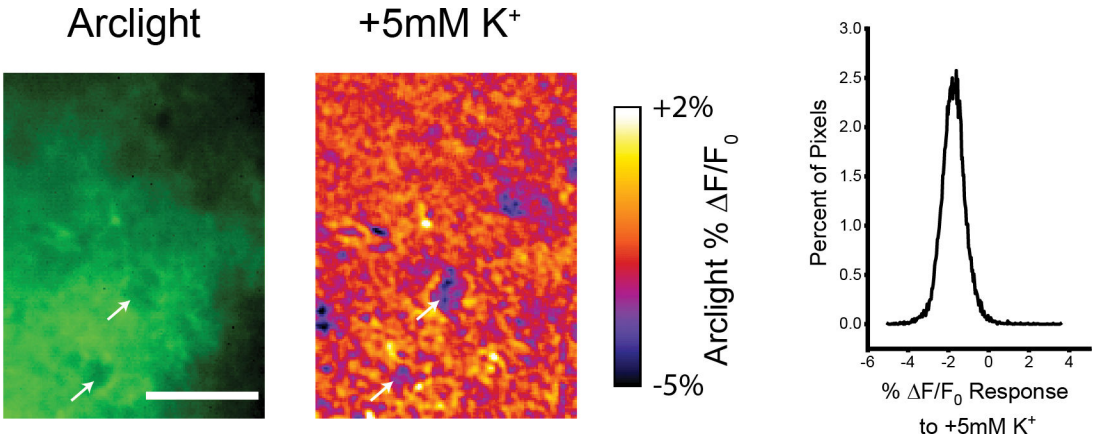


**Extended Data Fig. 6. $K^+$ wash-on calibration induces uniform depolarization.**

Example image of Arclight (scale bar = 30 μm) and response image to +5mM K+ wash-on, shows largely uniform voltage response across the field. Outliers, such as those highlighted with white arrows, tend to be areas excluding the Arclight sensor such as somas, or blood vessels. Distribution of pixel responses to +5mM $K^+$ shows a uniform distribution of depolarization responses.

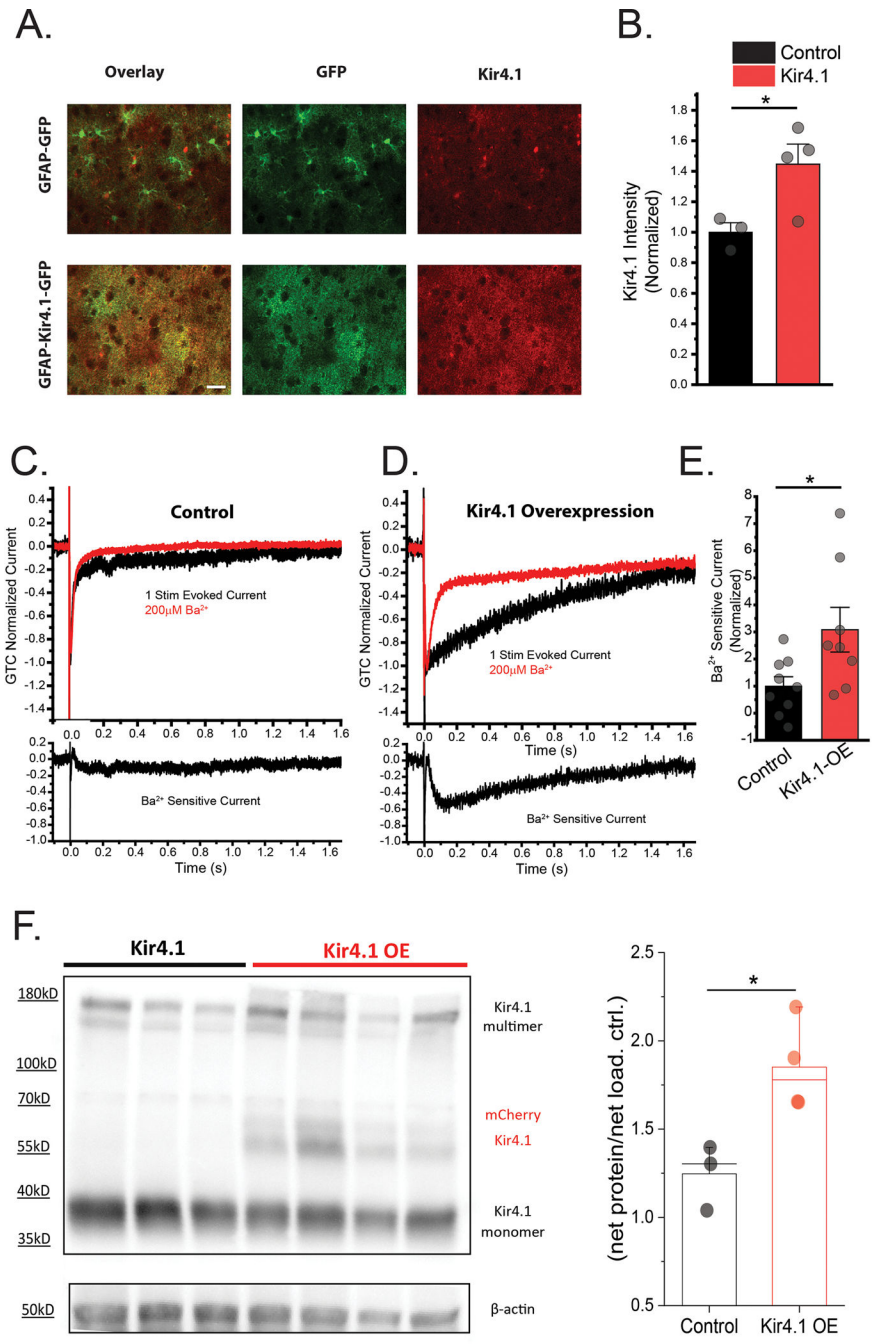


**Extended Data Fig. 7. Kir4.1 Overexpression.**

A) Confocal example image of immunofluorescence staining of Kir4.1 in Kir4.1 overexpression (Kir4.1-OE), (AAV5-GFAP-Kir4.1-EGFP) or control (AAV5-GFAP-GFP) infected cortex. B) Quantification of widefield Kir4.1 IHC staining shows significantly enhanced Kir4.1 staining. Scale bar = 50 μm. Two-sample t-test, n=3, 4 mice, p = 0.038. C, D) Astrocyte whole-cell voltage clamp shows enhanced $Ba^{2+}$ (Kir4.1 inhibitor) sensitive currents in Kir4.1-OE compared to control-infected cortex. 9 cells/3 mice each. E) $Ba^{2+}$- sensitive currents are significantly increase in Kir4.1-OE astrocytes, p =

0.028. F) Western blot quantification of Kir4.1-OE (AAV5-GFAP=Kir4.1-mCherry), shows significantly increased Kir4.1 protein compared to control virus (AAV5-GFAP-tdTomato). p = 0.049 * = p < 0.05 All panels: Error bars = Standard error of the mean.

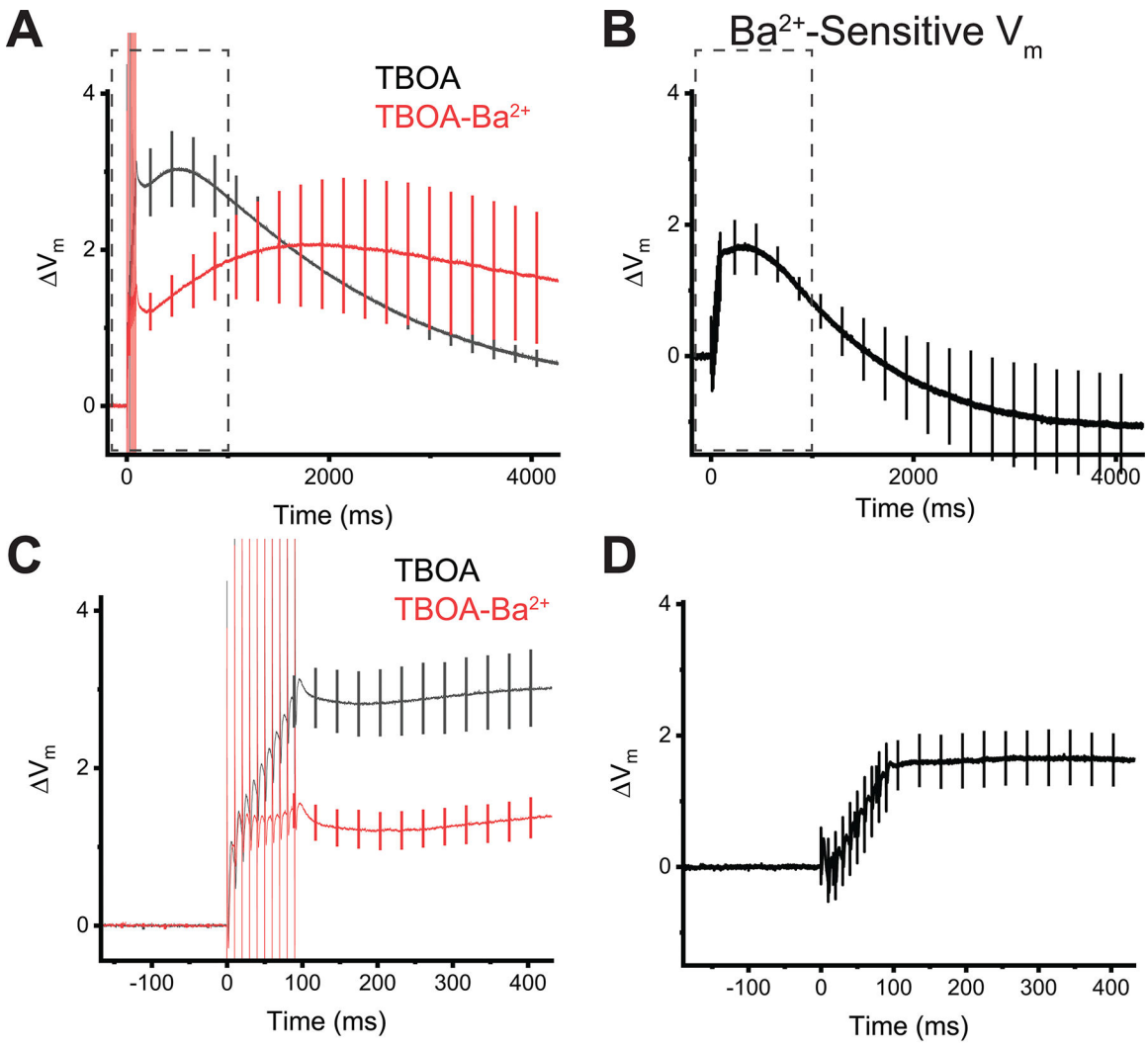


**Extended Data Fig. 8. Kir4.1 depolarizes astrocyte soma during neuronal activity.**

Astrocyte-whole cell current clamp recordings were made in the cortex to measure somatic $V_m$. In order to isolate the effects of Kir4.1 on astrocyte $V_m$ during neuronal activity, glutamate transporter activity was blocked with TFB-TBOA and responses to 10 stimuli at 100Hz were recorded before and after blockade of Kir4.1 with $Ba^{2+}$. A) Average paired traces before (black) and after (red) inhibition of Kir4.1 with $Ba^{2+}$, and B) the $Ba^{2+}$-sensitive $\Delta V_m$. These recordings show that Kir4.1 depolarizes astrocyte soma during neuronal activity. C and D) Expanded time scale (dashed boxes in A & B) to show $V_m$ during stimulus. N = 5 cells. All panels: Error bars = Standard error of the mean.

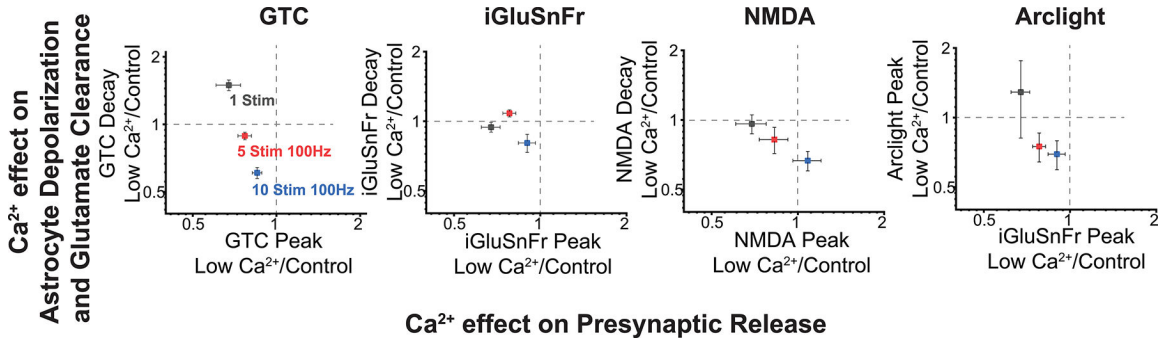


**Extended Data Fig. 9. The effects of low $Ca^{2+}$ on presynaptic release do not correlate with the effects on glutamate clearance and astrocyte depolarization.**

Utilizing data from figures 6, 7, and Ext. Fig. 10, we plotted the effects of Low $Ca^{2+}$ aCSF on presynaptic release (x-axis) and glutamate clearance/astrocyte depolarization (y-axis) for 1, 5, and 10 stimuli at 100Hz. In each condition, Low $Ca^{2+}$ is normalized to control. Dashed lines represent no change from control. Left of the dashed line on the x-axis represents a reduction in presynaptic release (as assayed by GTC, iGluSnFr, or NMDA peak amplitude). Beneath the dashed line represents an enhanced glutamate clearance/reduced depolarization (as assayed by GTC/iGluSnFr/NMDA decays and Arclight peaks). 1 Stim responses (grey) shows the largest change in presynaptic release, with the smallest effect on glutamate clearance/depolarization. 10 Stimuli at 100Hz (blue) shows the smallest presynaptic release effect with the largest glutamate clearance/depolarization effect.

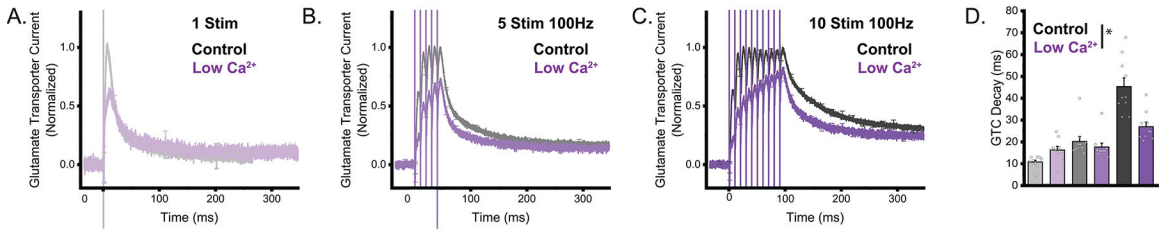


**Extended Data Fig. 10. Low $Ca^{2+}$ Glutamate Transporter Currents.**

Glutamate transporter currents were recorded from astrocytes with Control or Low $Ca^{2+}$ aCSF, showing enhanced glutamate clearance following trains of stimulation. Two way repeated measures ANOVA * = $p<0.05$. n = 10 cells/3 mice, p = 0.046. All panels: Error bars = Standard error of the mean.

## Supplementary Material

Refer to Web version on PubMed Central for supplementary material.

## Acknowledgements:

We thank members of the Dulla, Haydon, and Rios labs, Dr. Joseph Raimondo, and Dr. Jeffery Diamond for helpful comments on the manuscript. We thank Dr. Yongjie Yang (Tufts) for EAAT2-tdTomato mice. We thank Dr. Loren Looger (UCSD), Dr. Vincent Pieribone (Yale), Dr. Baljit Khakh (UCLA), and Dr. Sergio Grinstein (University of Toronto) for making plasmids and constructs available.

**Funding:**

This work was supported by the NIH (NS113499, NS104478, NS100796 to CGD).

## Data availability:

The datasets generated during and analyzed during the current study are available from the corresponding author on request.

## REFERENCES

1. Levy L, Warr O & Attwell D Stoichiometry of the glial glutamate transporter GLT-1 expressed inducibly in a Chinese hamster ovary cell line selected for low endogenous Na+-dependent glutamate uptake. The Journal of neuroscience 18, 9620–9628 (1998). [PubMed: 9822723]
2. Higashi K et al. An inwardly rectifying K(+) channel, Kir4.1, expressed in astrocytes surrounds synapses and blood vessels in brain. Am J Physiol Cell Physiol 281, C922–931, doi:10.1152/ajpcell.2001.281.3.C922 (2001). [PubMed: 11502569]
3. Amzica F & Neckelmann D Membrane capacitance of cortical neurons and glia during sleep oscillations and spike-wave seizures. J Neurophysiol 82, 2731–2746, doi:10.1152/jn.1999.82.5.2731 (1999). [PubMed: 10561441]
4. Amzica F In vivo electrophysiological evidences for cortical neuron-glia interactions during slow (<1 Hz) and paroxysmal sleep oscillations. J Physiol Paris 96, 209–219 (2002). [PubMed: 12445898]
5. Ma B, Xu G, Wang W, Enyeart JJ & Zhou M Dual patch voltage clamp study of low membrane resistance astrocytes in situ. Mol Brain 7, 18, doi:10.1186/1756-6606-7-18 (2014). [PubMed: 24636341]
6. Armbruster M, Hanson E & Dulla CG Glutamate Clearance Is Locally Modulated by Presynaptic Neuronal Activity in the Cerebral Cortex. J Neurosci 36, 10404–10415, doi:10.1523/JNEUROSCI.2066-16.2016 (2016). [PubMed: 27707974]
7. Pinky NF, Wilkie CM, Barnes JR & Parsons MP Region- and Activity-Dependent Regulation of Extracellular Glutamate. J Neurosci 38, 5351–5366, doi:10.1523/JNEUROSCI.3213-17.2018 (2018). [PubMed: 29760178]
8. Piatkevich KD et al. A robotic multidimensional directed evolution approach applied to fluorescent voltage reporters. Nat Chem Biol 14, 352–360, doi:10.1038/s41589-018-0004-9 (2018). [PubMed: 29483642]
9. Jin L et al. Single action potentials and subthreshold electrical events imaged in neurons with a fluorescent protein voltage probe. Neuron 75, 779–785, doi:10.1016/j.neuron.2012.06.040 (2012). [PubMed: 22958819]
10. Lee Y, Messing A, Su M & Brenner M GFAP promoter elements required for region-specific and astrocyte-specific expression. Glia 56, 481–493, doi:10.1002/glia.20622 (2008). [PubMed: 18240313]
11. Yang Y et al. Molecular comparison of GLT1+ and ALDH1L1+ astrocytes in vivo in astroglial reporter mice. Glia 59, 200–207 (2011). [PubMed: 21046559]
12. Miesenbock G, De Angelis D & Rothman J Visualizing secretion and synaptic transmission with pH-sensitive green fluorescent proteins. Nature 394, 192–195 (1998). [PubMed: 9671304]
13. Koivusalo M et al. Amiloride inhibits macropinocytosis by lowering submembranous pH and preventing Rac1 and Cdc42 signaling. J Cell Biol 188, 547–563, doi:10.1083/jcb.200908086 (2010). [PubMed: 20156964]
14. Shigetomi E et al. Imaging calcium microdomains within entire astrocyte territories and endfeet with GCaMPs expressed using adeno-associated viruses. J Gen Physiol 141, 633–647, doi:10.1085/jgp.201210949 (2013). [PubMed: 23589582]
15. Mukamel EA, Nimmerjahn A & Schnitzer MJ Automated analysis of cellular signals from large-scale calcium imaging data. Neuron 63, 747–760, doi:10.1016/j.neuron.2009.08.009 (2009). [PubMed: 19778505]

16. Savtchenko LP et al. Disentangling astroglial physiology with a realistic cell model in silico. Nat Commun 9, 3554, doi:10.1038/s41467-018-05896-w (2018). [PubMed: 30177844]
17. Heinemann U & Lux HD Ceiling of stimulus induced rises in extracellular potassium concentration in the cerebral cortex of cat. Brain Res. 120, 231–249 (1977). [PubMed: 832122]
18. Olsen ML & Sontheimer H Functional implications for Kir4.1 channels in glial biology: from K+ buffering to cell differentiation. J Neurochem 107, 589–601, doi:10.1111/j.1471-4159.2008.05615.x (2008). [PubMed: 18691387]
19. Olsen ML, Higashimori H, Campbell SL, Hablitz JJ & Sontheimer H Functional expression of Kir4.1 channels in spinal cord astrocytes. Glia 53, 516–528, doi:10.1002/glia.20312 (2006). [PubMed: 16369934]
20. Tong X et al. Astrocyte Kir4.1 ion channel deficits contribute to neuronal dysfunction in Huntington's disease model mice. Nat Neurosci 17, 694–703, doi:10.1038/nn.3691 (2014). [PubMed: 24686787]
21. Cui Y et al. Astroglial Kir4.1 in the lateral habenula drives neuronal bursts in depression. Nature 554, 323–327, doi:10.1038/nature25752 (2018). [PubMed: 29446379]
22. Kelley KW et al. Kir4.1-Dependent Astrocyte-Fast Motor Neuron Interactions Are Required for Peak Strength. Neuron 98, 306–319 e307, doi:10.1016/j.neuron.2018.03.010 (2018). [PubMed: 29606582]
23. Djukic B, Casper KB, Philpot BD, Chin LS & McCarthy KD Conditional knock-out of Kir4.1 leads to glial membrane depolarization, inhibition of potassium and glutamate uptake, and enhanced short-term synaptic potentiation. J Neurosci 27, 11354–11365, doi:10.1523/JNEUROSCI.0723-07.2007 (2007). [PubMed: 17942730]
24. Hille B Ion channels of excitable membranes. 3rd edn, (Sinauer Associates, 2001).
25. Diamond J Deriving the glutamate clearance time course from transporter currents in CA1 hippocampal astrocytes: transmitter uptake gets faster during development. The Journal of neuroscience 25, 2906–2916 (2005). [PubMed: 15772350]
26. Marvin J et al. An optimized fluorescent probe for visualizing glutamate neurotransmission. Nature methods (2013).
27. Raimondo JV, Burman RJ, Katz AA & Akerman CJ Ion dynamics during seizures. Front Cell Neurosci 9, 419, doi:10.3389/fncel.2015.00419 (2015). [PubMed: 26539081]
28. Murphy-Royal C et al. Surface diffusion of astrocytic glutamate transporters shapes synaptic transmission. Nat.Neurosci. 18, 219–226 (2015). [PubMed: 25581361]
29. Shih PY et al. Retrograde synaptic signaling mediated by K+ efflux through postsynaptic NMDA receptors. Cell Rep 5, 941–951, doi:10.1016/j.celrep.2013.10.026 (2013). [PubMed: 24268779]
30. Sancho L, Contreras M & Allen NJ Glia as sculptors of synaptic plasticity. Neurosci Res 167, 17–29, doi:10.1016/j.neures.2020.11.005 (2021). [PubMed: 33316304]
31. Letellier M et al. Astrocytes regulate heterogeneity of presynaptic strengths in hippocampal networks. Proc Natl Acad Sci U S A 113, E2685–2694, doi:10.1073/pnas.1523717113 (2016). [PubMed: 27118849]
32. D'Ascenzo M et al. Electrophysiological and molecular evidence of L-(Cav1), N- (Cav2.2), and R-(Cav2.3) type Ca2+ channels in rat cortical astrocytes. Glia 45, 354–363, doi:10.1002/glia.10336 (2004). [PubMed: 14966867]
33. Sontheimer H, Black JA & Waxman SG Voltage-gated Na+ channels in glia: properties and possible functions. Trends Neurosci 19, 325–331, doi:10.1016/0166-2236(96)10039-4 (1996). [PubMed: 8843601]
34. Wan X et al. Bimodal voltage dependence of TRPA1: mutations of a key pore helix residue reveal strong intrinsic voltage-dependent inactivation. Pflugers Arch 466, 1273–1287, doi:10.1007/s00424-013-1345-6 (2014). [PubMed: 24092046]
35. Lalo U, Pankratov Y, Kirchhoff F, North RA & Verkhratsky A NMDA receptors mediate neuron-to-glia signaling in mouse cortical astrocytes. J Neurosci 26, 2673–2683, doi:10.1523/JNEUROSCI.4689-05.2006 (2006). [PubMed: 16525046]
36. Willford SL, Anderson CM, Spencer SR & Eskandari S Evidence for a Revised Ion/Substrate Coupling Stoichiometry of GABA Transporters. J Membr Biol 248, 795–810, doi:10.1007/s00232-015-9797-6 (2015). [PubMed: 25824654]

37. Octeau JC et al. Transient, Consequential Increases in Extracellular Potassium Ions Accompany Channelrhodopsin2 Excitation. Cell Rep 27, 2249–2261 e2247, doi:10.1016/j.celrep.2019.04.078 (2019). [PubMed: 31116972]

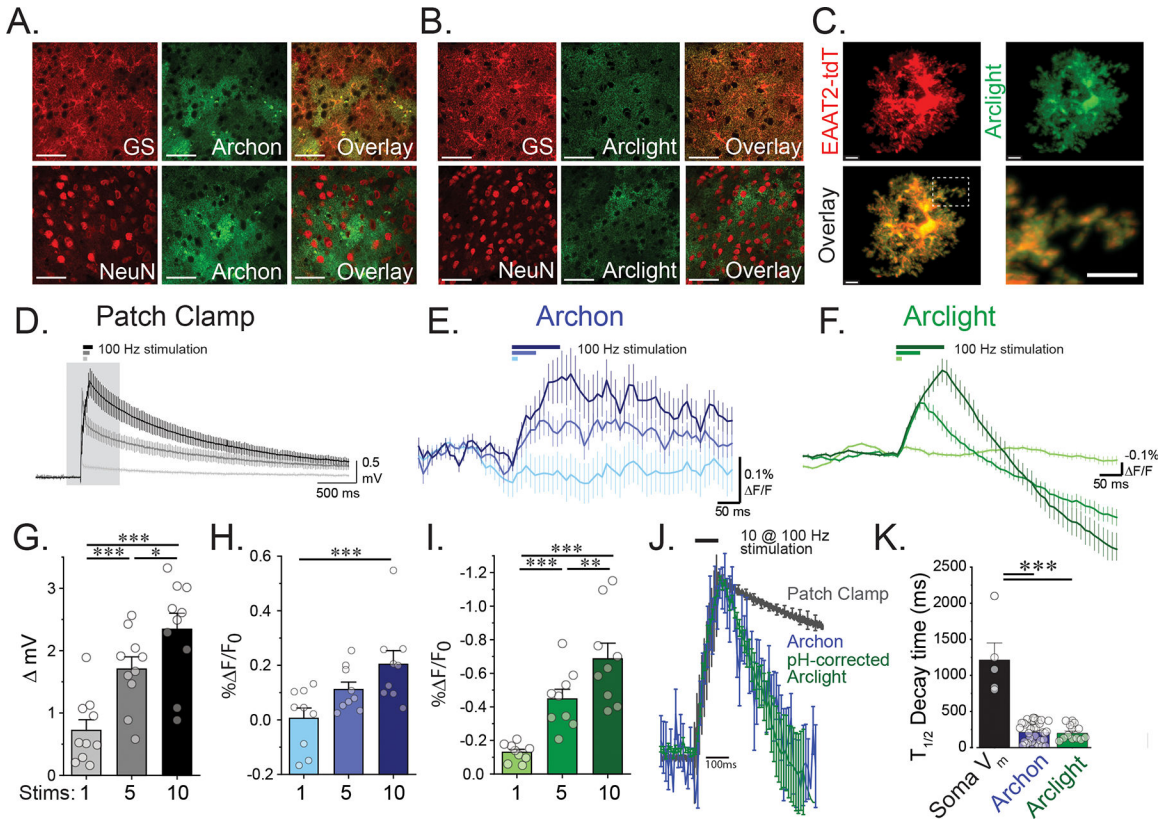


**Figure 1: Astrocyte GEVI imaging enables measuring astrocyte PAP $V_m$ changes.**

IHC of astrocyte expression of the GEVIs A) Archon (AAV5-GFAP-Archon) or B) Arclight (AAV5-GFAP-Arclight) show astrocyte specific expression with colocalization with the astrocyte marker glutamine synthase (GS) and lack of colocalization with the neuronal marker NeuN. Scale Bar = 50 μm, repeated for 3 mice in each condition. C) Astrocyte reconstruction based on the astrocyte reporter line EAAT2-tdtomato, shows that Arclight GEVI labels the full astrocytic arbor. Scale bar: 5 μm, Inset 5 μm. (See Extended Figure 2 for additional reconstructions). D) Whole-cell current clamp recordings of astrocyte $\Delta V_m$ in response to 1, 5, or 10 Stimuli at 100Hz. Gray box marks time-scale for astrocyte GEVI responses to the same stimuli for E) Archon or F) Arclight. G) Whole cell recording, H) Archon, and I) Arclight show progressive depolarizations for increased stimuli number at 100Hz. (1 way repeated measures ANOVA; Tukey post test; G: 1 v 5 stim p = 2.1E-4, 1 v 10 stim p = 3.1E-7, 5 v 10 stim p = 0.010; H: 1 v 5 stim p = 0.051, 1 v 10 stim p = 5.3E-4, 5 v 10 stim p = 0.093; I: 1 v 5 stim p = 7.7E-4, 1 v 10 stim p = 1.3E-6, 5 v 10 stim p = 0.0083) J) Normalized overlay of 10 Stimuli 100Hz responses of Patch Clamp, Archon, and Arclight-pH corrected decays shows significantly faster decays K) for GEVI assays compared to patch-clamp. n = 5 cells/3 mice (Patch Clamp); n = 33 slices/8 mice (Archon); n = 11 slices/3 mice (Arclight). (1 Way ANOVA, Tukey post test, Soma $V_m$ v Archon p < 1E-11, Soma $V_m$ v Arclight p < 1E-11, Archon v Arclight p = 0.98), * = p<0.05, ** = p<0.01, *** = p<0.001. All panels: Error bars = Standard error of the mean.

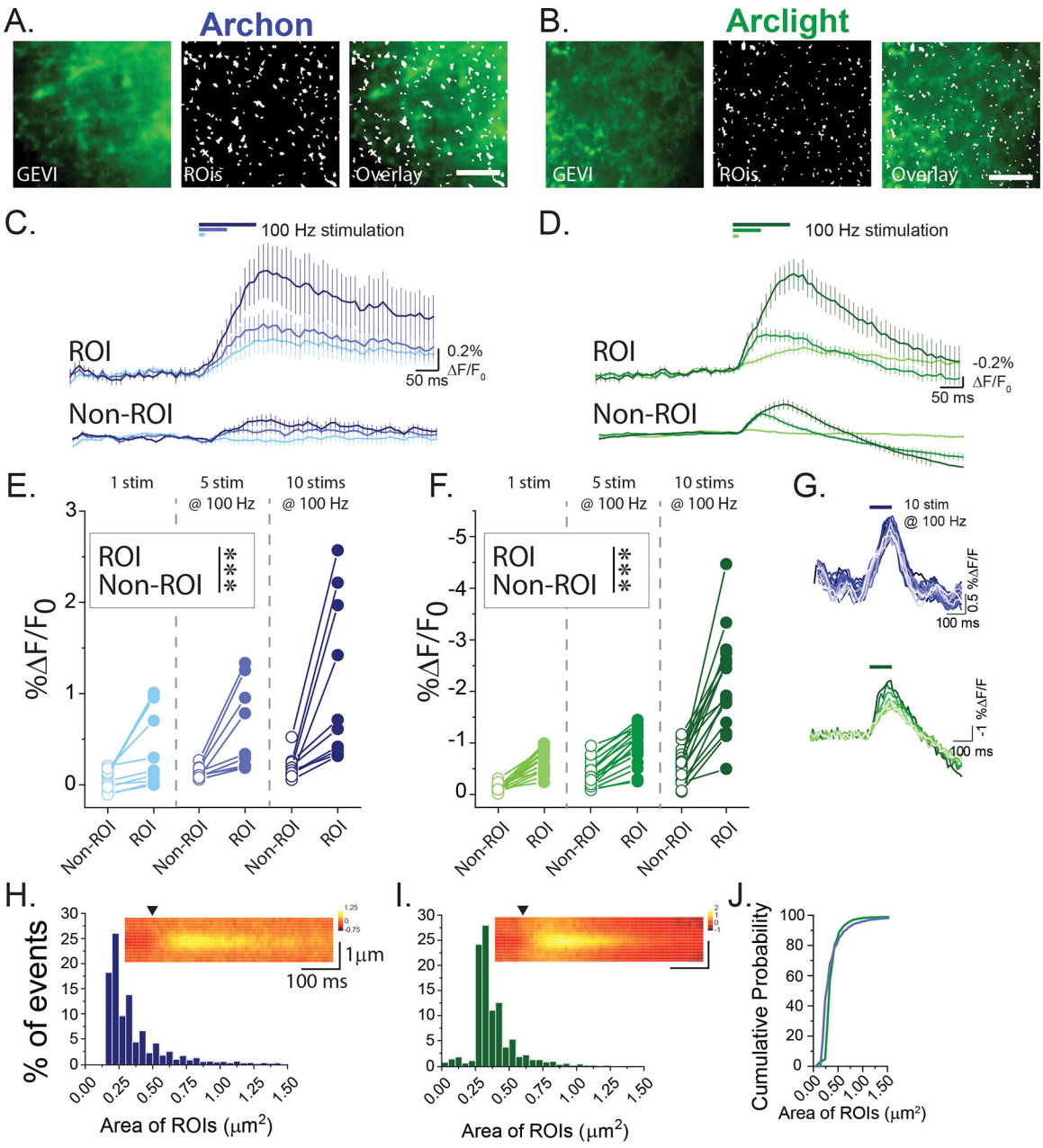


**Figure 2: Astrocyte GEVI shows microdomain depolarizations.**

A) Archon GEVI colabel (GFP) and ROI maps based on 10 Stimuli at 100Hz responses show small and distributed ROIs. B) Arclight (basal fluorescence) and ROI maps shows small and distributed ROIs. Scale bar = 10 μm. Average traces of ROI and Non-ROI regions from C) Archon and D) Arclight in response to 1, 5, and 10 Stimuli at 100Hz. E) Archon and F) Arclight ROIs show significantly enhanced responses ($\Delta F/F_0$). n = 10 slices/5 mice (Archon), n = 17 slices/6 mice (Arclight). Two way repeated ANOVA, Tukey post test Archon ROI v Non-ROI p = 9.9E-5; Arclight ROI v Non-ROI p = 6.3E-8, *** = p<0.001 G) Single slice examples of repeated 10 Stimuli 100Hz trains shows stable GEVI responses across multiple rounds of stimulation. Distribution of ROI sizes for H) Archon and I)

Arclight shows small responsive areas and average kymographs shows spatially restricted areas of depolarization. Black arrowheads indicate time of stimulation. J) Both GEVIs show similar size distributions. All panels: Error bars = Standard error of the mean.

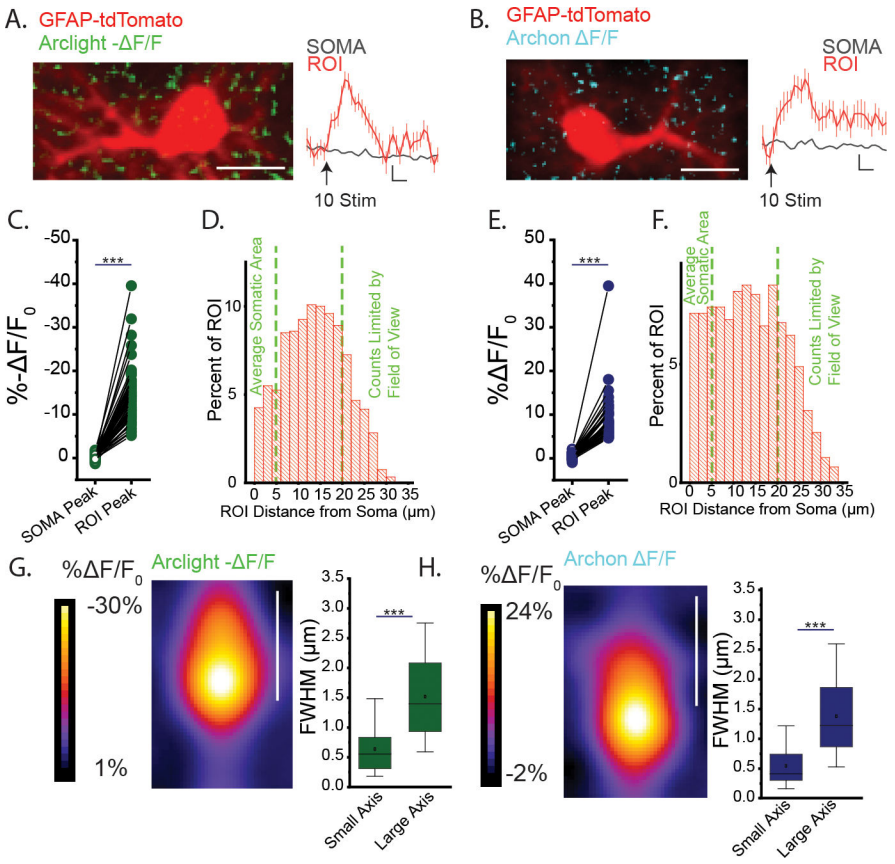


**Figure 3: Astrocyte GEVI depolarization microdomains occur outside of astrocyte somas and primary processes.**

A) Arclight GEVI co-expressed with GFAP-tdTomato to label astrocyte soma and primary processes. Example image of Arclight −ΔF/F in response to 10 Stimuli at 100Hz show that hotspots localize outside of astrocyte soma and primary processes. Example trace of single slice shows Arclight ROI and soma response. Scale bar = 10 μm. Trace scale bars −2% $\Delta F/F_0$, 200 ms. B) Archon GEVI co-expressed GFAP-tdTomato as in A). Example image of Archon ΔF/F hotspots localize outside of astrocyte soma and primary processes. Example trace of Archon response of ROI and soma. Scale bar = 10 μm. Trace scale bars 2% $\Delta F/F_0$, 200 ms. C) Peak Arclight $-\Delta F/F_0$ response shows significantly enhanced response of ROIs compared to soma. Paired t-test. N = 59 Astrocytes from 4 mice p = 3.1E-24. D) Histogram of Arclight ROI distances from soma center of mass, shows broad distribution of ROIs throughout the astrocyte arbor. E) Peak Archon $\Delta F/F_0$ response shows significantly enhanced response of ROIs compared to soma. Paired t-test. N = 47 Astrocytes from 3 mice. p = 1.4E-14. F) Histogram of Archon ROI distances from soma center of mass, shows broad distribution of ROIs throughout the astrocyte arbor. G) Arclight ROIs are aligned and overlayed and peak ROI visualized. ROIs shows asymmetry with a long and short axis. Scale bar = 1 μm, 432 ROIs from 4 mice. p = 9.2E-107 H) Archon ROIs are aligned and overlayed and peak ROI visualized. ROIs show shows asymmetry with a long and short axis. 530 ROIs from 3 mice. Paired two-sample t-test p = 1.3E-128 *** = p < 0.001. Box-Whisker plot, Box = 25, 50, 75$^{th}$ percentile, whiskers = 5–95$^{th}$ percentile, square = mean.

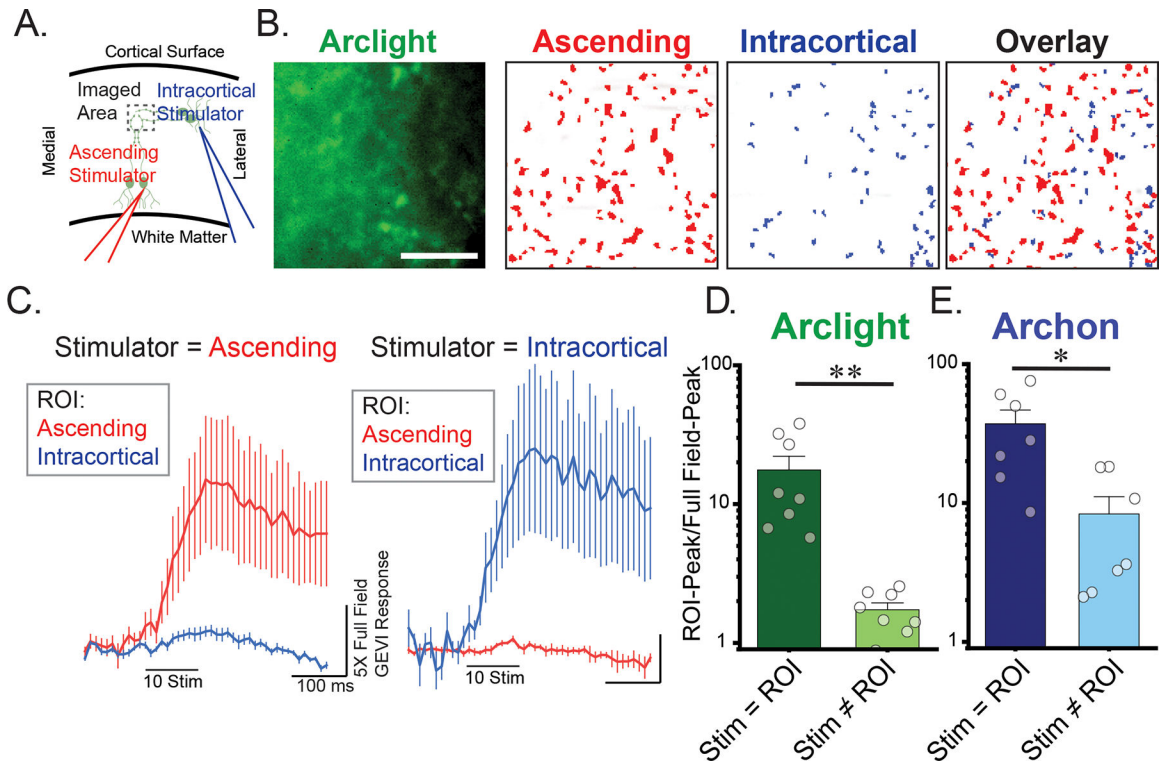


**Figure 4: Pathway independence of astrocyte depolarization.**

A) To test pathway specificity we utilized an ascending stimulator (Red) and an intracortical stimulator (Blue). B) Example ROI maps of Ascending and Intracortical stimulators show little overlap. Scale bare = 10 μm. C) Average Arclight traces of matched ROI (Stim: Ascending and ROI: Ascending) or (Stim: Intracortical and ROI: Intracortical) or unmatched. D) Arclight and E) Archon matched ROI shows significant enhancement of PAP $\Delta F/F_0$ over unmatched suggesting pathway specificity. Log-scale. n = 8 slices/ 3 mice (Arclight p = 0.0033); n = 7 slice/3 mice (Archon p = 0.021) Paired t-test * = $p<0.05$; ** = $p<0.01$. All panels: Error bars = Standard error of the mean.

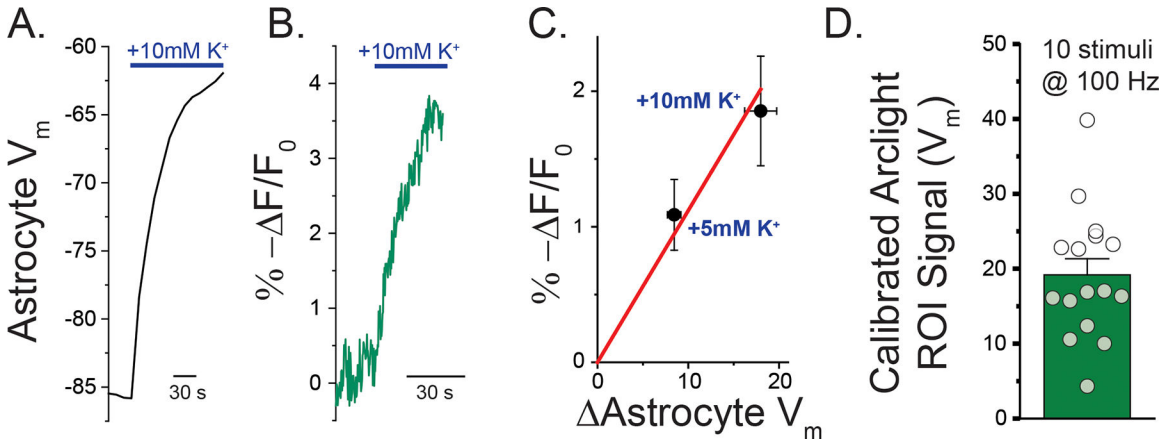


**Figure 5: Calibrating Arclight-GEVI.**

Example traces of A) Astrocyte whole-cell recordings and B) Arclight GEVI show depolarizations in control (2.5mM K+ aCSF) and in response to addition of high $K^+$ to the aCSF (+10mM $K^+$). C) Correlation between whole-cell $\Delta V_m$ changes and Arclight $\Delta F/F_0$, in response to addition of +5mM and +10mM $K^+$ to the aCSF solutions and fit with line going through the origin (red). Arclight N = 7 slices/3 animals per condition, Whole-cell 8 cells/3 animals per condition. D) Arclight fluorescence peak ROI response to 10 stimuli at 100Hz mapped to $\Delta V_m$ using the calibration. N = 17 slices/6 mice. All panels: Error bars = Standard error of the mean.

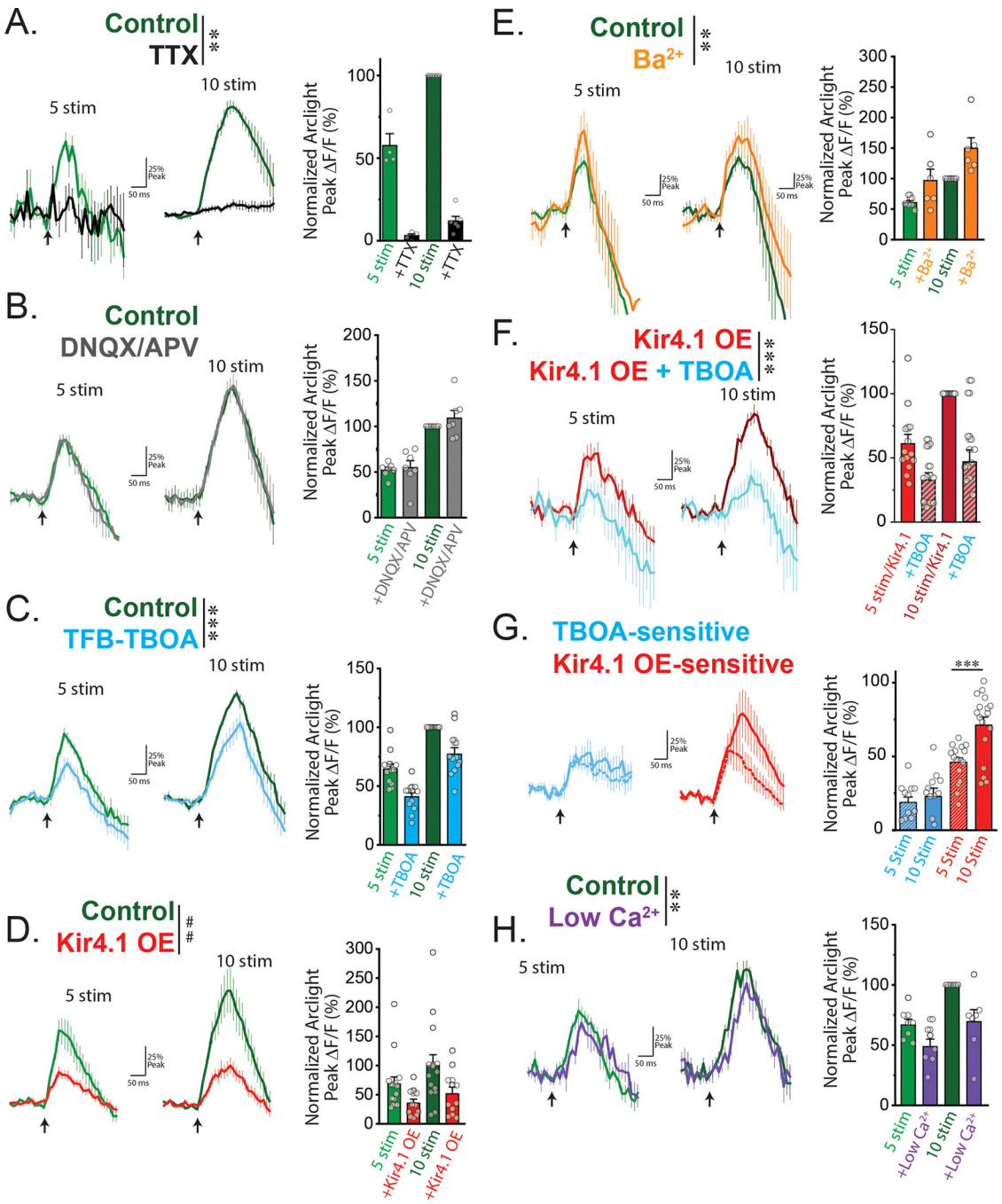


**Figure 6: Glutamate transport and increases in $[K^+]_e$ contribute to astrocyte depolarization.**

Arclight GEVI imaging in response to 5 and 10 stimuli at 100Hz. A) TTX abolishes the GEVI response. n = 6 slices/3 mice p = 1.3E-4. B) Post-synaptic glutamate receptors blockers DNQX and APV have no effect on the peak GEVI response. n = 7 slices/3 mice, p = 0.89. C) The EAAT inhibitor TFB-TBOA reduces the peak GEVI signal for 5 and 10 stimuli. n = 13 slices/3 mice, p = 6.9E-5. D) Overexpressing the astrocytic potassium channel Kir4.1, Kir4.1-OE, significantly reduces the GEVI depolarization peak. n = 15 slices/5 mice (control); n = 11 slices/4 mice (Kir4.1-OE), p = 0.0056. E) Inhibiting Kir4.1

with 200uM $Ba^{2+}$ enhances the GEVI signal. n = 6 slices/3 mice, p = 0.0041. F) TFB-TBOA reduces the Arclight GEVI peaks of Kir4.1-OE astrocytes, showing the effects are additive. n = 13 slices/3 mice, p = 9.9E-5. G) Average TFB-TBOA-sensitive and Kir4.1-OE-sensitive traces. TFB-TBOA-sensitive effect does not increase from 5 to 10 stimuli, while the Kir4.1-OE-sensitive effects are enhanced with additional stimuli. Paired t-test, p = 0.54, p = 3.7E-7. I) Reducing extracellular $Ca^{2+}$, reduces the peak Arclight signal. n = 7 slices/3 mice, p = 0.0093. Two Way ANOVA, Tukey post test ### = p<0.001. Two Way Repeated Measures ANOVA, Tukey post test ** = p<0.01, *** = p<0.001. All panels: Error bars = Standard error of the mean.

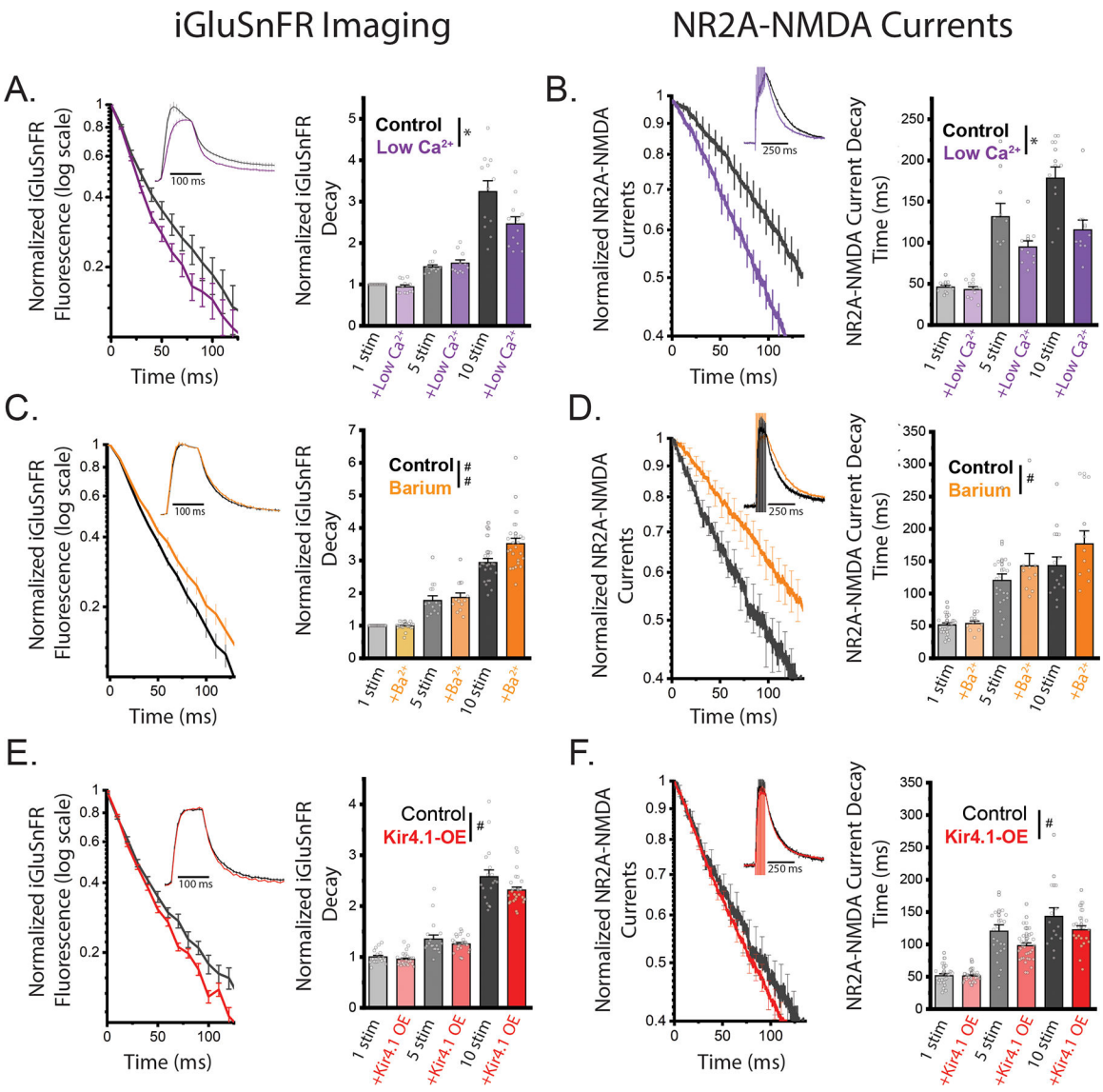


**Figure 7: Astrocyte depolarization contributes to activity dependent slowing of glutamate clearance.**

Glutamate clearance slowing, as assayed by single exponential fits to iGluSnFr imaging and NR2A-specific NMDA current decays in response to 1, 5 and 10 stimuli at 100Hz. A) Low $Ca^{2+}$ accelerates average iGluSnFr decay following 10 stimuli at 100Hz. Full trace inset. n = 12 slices/5 mice, p = 0.039.B) Average 10 stimuli 100Hz NR2A-NMDA current decay shows Low $Ca^{2+}$ aCSF speeds NR2A-NMDA current decay. Full trace inset. n = 10 cells/3 mice, p = 0.011C) Inhibiting Kir4.1 with 200 μM $Ba^{2+}$ slows iGluSnFr decay. n = 24 slices/6 mice p = 0.0086 D) Inhibiting Kir4.1 with 200 μM $Ba^{2+}$ prolongs NR2A-NMDA currents. n = 15 cells/3 mice (Control); 10 cells/4 mice ($Ba^{2+}$), p = 0.026. E) Kir4.1-Ovexpression accelerates iGluSnFr decay. n = 18 slices/3 mice (control) n = 27 slices/4 mice (Kir4.1-OE), p = 0.010. F) Kir4.1-Overexpression speeds NR2A-NMDA current decay. n = 33 cells/4 mice, control same as D, p = 0.046. Two Way ANOVA # =

p<0.05, ### = p<0.001. Two Way Repeated Measures ANOVA * = p<0.05, ** = p<0.01. All panels: Error bars = Standard error of the mean.